

CO₂ Hydrogenation Over Bulk and Loaded NiFe Catalysts: The Effect of Carrier



A. G. Dyachenko , O. V. Ischenko , V. E. Diyuk , S. V. Gaidai ,
A. V. Yatsymyrskiy , O. V. Pryhunova , O. V. Goncharuk ,
M. V. Borysenko , O. V. Mischanchuk , Olga Niemiec ,
and V. V. Lisnyak 

Abstract The structure and surface properties of bulk and loaded bimetallic nickel–iron (NiFe) catalysts were studied in detail by various characterization technologies, such as X-ray diffraction, scanning electron microscopy, nitrogen porosimetry, temperature-programmed reduction, and temperature-programmed desorption mass spectrometry. We demonstrate the dependence of the catalytic activity of bulk NiFe catalysts against the Ni/Fe ratio. Based on the experimental observations, the possible mechanism of carbon dioxide (CO₂) hydrogenation to methane (CH₄) on the surface of the active bulk catalyst and that loaded on carbon nanotubes was proposed. The CO₂ conversion and CH₄ selectivity mainly depend on the nature of the carrier. Based on the example of the catalysts loaded on carbon carriers, the effect of surface morphology on the CO₂ conversion and CH₄ selectivity is shown. We showed the role of the initial carriers, namely, crystal structure, texture, and surface morphology, on the formation of active sites of nanocomposite NiFe catalysts based on the alumina with different porosities.

A. G. Dyachenko (✉) · M. V. Borysenko · O. V. Mischanchuk
Chuiiko Institute of Surface Chemistry, National Academy of Sciences of Ukraine, Kyiv 03164,
Ukraine
e-mail: dyachenko.alla@yahoo.com

O. V. Ischenko · V. E. Diyuk · S. V. Gaidai · A. V. Yatsymyrskiy · O. V. Pryhunova · V. V. Lisnyak
Taras Shevchenko National University of Kyiv, Kyiv 01601, Ukraine

O. V. Goncharuk
National Technical University of Ukraine, Igor Sikorsky Kyiv Polytechnic Institute, Kyiv 03056,
Ukraine

A. G. Dyachenko · O. Niemiec
Institute of Physical Chemistry, Polish Academy of Sciences, 01-224 Warsaw, Poland

1 Introduction

Methanation of carbon dioxide (CO_2) with electrolytically generated hydrogen (H_2) from renewable energies enables chemical energy storage in a cycle [1] and contributes to the decrease of atmospheric CO_2 pollution [1–3]. Production of synthetic natural gas is of increased interest since it can easily be stored and transported in the existing gas infrastructure while being reused for energy generation [4]. Using bimetallic bulk catalysts in the methanation reaction is much more efficient than monometallic ones [5–9]. Adding the iron component to the traditional monometallic nickel catalyst significantly improves the conversion of CO_2 and increases the yield of the target product—methane (CH_4). At the same time, the iron amount should be regulated to prevent the formation of undesirable co-products, such as carbon monoxide (CO) [5, 6, 9, 10]. Finding the optimal ratio between the active components in the composition of the bulk NiFe catalysts is a crucial step in the study of their effectiveness in the CO_2 methanation reaction and the determination of the mechanism of CH_4 formation [5]. In the future, this directed us to use these compositions as part of the loaded catalysts. It is possible to increase the contact surface with reagent molecules by increasing the dispersion of the active mass of the catalyst by applying a certain amount of the active component to the surface of the carrier [10–12]. In addition, the catalyst carrier participates in heterogeneous catalytic processes by creating additional sites for the adsorption of molecules from the gas phase [13]. The most popular oxide carriers for the methanation reactions are silica (SiO_2) and alumina (Al_2O_3) [10, 11, 13, 14]. An important characteristic of oxide carriers is their porosity, which affects the distribution and localization of the deposited metal phase. For example, the microporous structure of titanium oxide blocks the ability of active metals in the micropores to react with molecules from the gas phase. Although TiO_2 is an active catalyst for many environmental processes [15, 16], including the photocatalytic reduction of CO_2 [17]. Also, in the process of synthesis of catalysts loaded on oxide carriers, it is possible for the carrier to interact with metals and the formation of spinels. Such interaction is not always beneficial for the reaction catalyst because it can provoke the formation of by-products. Carbon-based supports are an excellent alternative to oxides. Carbon nanotubes [18–21], graphite materials [22], and activated carbon [23] have a good surface area; their pore structures can be adjusted, thus favoring a lower interaction with the active metallic catalyst due to its inert characteristic. The carbon-based support can promote the formation of Met_xC_y , which is not an active phase for the methanation process and typically deactivates the catalytic metal sites [24].

We found some factors influencing catalyst efficiency, including the effects of (i) the ratio of components in the active NiFe phase; (ii) the amount of the active NiFe phase in the composition of the loaded catalyst; and (iii) the nature of the carrier.

Nevertheless, we found that in addition to these factors, the carrier structure plays a significant role [25, 26]. We have determined that the mechanism of methane formation on the surface of bulk and deposited catalysts is different [5, 6, 27, 28]. The nature of the carrier surface influences the formation of intermediate products of the reaction

and the catalytic performance of the catalysts [11, 13, 28]. The pore size distribution in oxide carriers determines the catalytic performance and the reaction product distribution. It can profoundly affect the dispersion and reducibility of catalytic metals and regulate the mass transport performance. In this line, the increasing catalyst pore sizes lead to higher ratios of C₂⁺ formation due to the enhancement of product diffusion. A narrow distribution of pore sizes limits the particle size of catalytic metals that prevents the C–C bond growth [29, 30]. All these factors affect the CO₂ conversion efficiency and selectivity toward CH₄, regulating the CH₄ formation mechanism.

In this study, we have compared the catalytic performance in the CO₂ methanation of the bulk and loaded NiFe catalysts and have conducted a comparative analysis of the effect of different carriers on the CH₄ formation process.

2 Experimental

2.1 Synthesis of Bulk NiFe Catalysts

To study the catalytic activity of the bulk NiFe catalysts in the CO₂ hydrogenation reaction, samples with a specified weight ratio of Ni and Fe metals were synthesized by the method of decomposition of metal salts. The synthesis of these catalysts can be conventionally divided into three stages. At the first stage, the calculated amounts of individual metals in a given ratio are subjected to co-dissolution in excess of nitric acid during heating. In the process of gradual evaporation of the solution, hydroxides of the corresponding metals are formed, and their subsequent thermal degradation leads to the formation of metal oxides, which are precursors of catalysts. The second stage is the reduction of the obtained oxides in the H₂/He gas flow at the temperature determined by the thermoprogrammed reduction (TPR) method [5]. The final stage is the formation of active sites of the catalyst in the reaction medium. This stage is carried out directly in the reactor before the study of catalytic activity.

2.2 Synthesis of Loaded NiFe Catalysts

Loading the active mass on the carriers was carried out by wet impregnation. The principle of the wet impregnation method consists of the delivery of cations forming the active metal catalyst to the carrier surface by ion sorption from water-soluble metal salts with subsequent removal of the solvent and thermal decomposition of adsorbed anions. As a result, we get a composite in which particles of transition metal oxides are localized on the surface of the carrier. These oxide particles are the precursors of the final product, namely, mono- or bimetallic catalyst loaded on the carrier surface. To form a catalytically active compound, the active transition metals were dissolved in concentrated nitric acid, similar to the procedure used to prepare

massive metal catalysts. For loading onto the surface of the carrier, a nitrate solution with 80 wt% of Ni and 20 wt% of Fe was prepared. The mass of the carrier was impregnated with the nitrate solution in order to obtain the amount of loaded active mass of 5–20 wt%. The obtained wet substance was dried in a sand bath at 150 °C and then calcined at 250–300 °C for a day.

Further formation of the catalyst was carried out by reducing with hydrogen gas in helium gas flow at the selected reduction temperature determined by the temperature-programmed reduction method with a reducing hydrogen gas (H_2) made to flow across the catalyst under gradually increasing thermal conditions (H_2 -TPR).

2.3 Temperature-Programmed Reduction (H_2 -TPR)

The reducibility of the NiFe catalysts (bulk and supported on different carriers) was studied with H_2 -TPR using thermal analysis. The thermograms were recorded using a Derivatograph Q-1500D (MOM, Hungary) operated in the temperature range of 50–600 °C at a heating rate of 5 °C/min. Experiments were conducted with 30–50 mg of sample loaded in an alumina crucible with a bottom perforated with small holes and covered with a perforated lid.

2.4 Textural Characterization

Nitrogen adsorption–desorption isotherms were measured on an ASAP 2405N adsorption analyzer at 77.4 K. Before adsorption measurements, the samples were outgassed at 110 °C for 2 h in a vacuum chamber. The standard Brunauer–Emmett–Teller (BET) method [31, 32] was used to calculate the specific surface area (S_{BET}). The total pore volume V_p was evaluated by converting the volume of adsorbed N_2 at the relative equilibrium adsorption pressure of 0.98–0.99, to the volume of liquid nitrogen per gram of adsorbent. Textural parameters: microporous, macroporous, and mesoporous surface areas (S_{micro} , S_{macro} , and S_{meso}), microporous, mesoporous, and macroporous volumes (V_{micro} , V_{meso} , V_{macro} , and V_p), and the average pore radius $R_{p,v}$ were found as in [13].

2.5 X-Ray Powder Diffraction (XRD)

X-ray diffraction (XRD) patterns of metal oxide (as-synthesized) and metal NCs (after testing in the catalytic process) were recorded on a DRON-3M powder diffractometer with monochromatic $CuK\alpha$ radiation ($\lambda = 0.15418$ nm) and $CoK\alpha$ radiation ($\lambda = 0.17903$ nm) over an angular range from 10° to 80°. X-ray tube operation parameters: voltage of 40 kV, current of 15 mA, scanning speed 2° min^{-1} . Interpretation of

the phase composition was performed using the integrated X-ray powder diffraction software suite PDXL from <https://www.rigaku.com/support/software/pdxl>. The crystalline structure of samples was analyzed using the JCPDS Database (International Center for Diffraction Data, PA, 2001). The average sizes of nanosized crystallites (d , nm) were estimated according to the Scherrer equation [33].

2.6 Scanning Electron Microscopy (SEM)

The images of uncoated samples of bulk or supported catalysts were captured on a Tescan Mira 3 GMU LV-FE-scanning electron microscope equipped with an energy dispersion X-ray (EDX) spectrometer from Oxford Instruments. The microscope was used in the back-scattered electron (BSE) mode to capture high-quality BSE SEM images with the INCA software.

The chemical analysis was carried out by collecting the EDX spectra from the selected areas with an Oxford INCA system. A ZAF procedure was used to calculate the concentration of analyzed elements from an X-ray spectrum emitted by a solid sample bombarded with a focused beam of electrons to obtain a localized chemical analysis with the EDX detector.

2.7 Catalytic Evaluation

The catalytic performances were studied in a flow reactor at atmospheric pressure [5, 13]. The reaction gas mixture consisted of 2 vol% CO₂, 55 vol% H₂, and 43 vol% He (helium was used as a carrier gas). The total gas flow rate was 0.1 l/min, and the catalyst weight was 1 g. The reaction components and products were monitored using a Shimadzu GC-2014 gas chromatograph equipped with a thermal conductivity detector. A column filled with 5A molecular sieves was used to separate the gas mixture components.

As a rule, the catalytic experiment was carried out in two heating modes. During the first heating, the catalyst was worked in the reaction mixture with the formation of active sites of the catalyst surface. This stage is considered by us to be the final stage of catalyst synthesis. During the second heating, the catalytic performance of the sample under study was directly determined. Equations (1–3) [13] were used to calculate the CO₂ conversion and the CH₄ and CO yields:

$$X_{\text{CO}_2} = \left(1 - \frac{[\text{CO}_2]_{\text{out}}}{[\text{CO}_2]_{\text{out}} + [\text{CH}_4]_{\text{out}} + [\text{CO}]_{\text{out}}} \right) \times 100\%, \quad (1)$$

$$Y_{\text{CH}_4} = \frac{[\text{CH}_4]_{\text{out}}}{[\text{CO}_2]_{\text{out}} + [\text{CH}_4]_{\text{out}} + [\text{CO}]_{\text{out}}} \times 100\%, \quad (2)$$

$$Y_{\text{CO}} = \frac{[\text{CO}]_{\text{out}}}{[\text{CO}_2]_{\text{out}} + [\text{CH}_4]_{\text{out}} + [\text{CO}]_{\text{out}}} \times 100\%, \quad (3)$$

where $[\text{CO}_2]_{\text{out}}$, $[\text{CO}]_{\text{out}}$, and $[\text{CH}_4]_{\text{out}}$ are the volume percentages (vol%) of CO_2 , CO , and CH_4 gases, correspondingly, in gas mixtures sampled at the reactor outlet.

2.8 TPD MS Investigation

After the catalytic experiment completion, when reaching maximum CO_2 conversion, the reactor with the catalyst was cooled to room temperature [13, 34]. Under such conditions, the catalyst surface contains adsorbed particles formed during the reaction at the stage of maximum CO_2 conversion and the highest methane yield.

During the course of TPD MS studies, a small catalyst amount was transferred to a quartz cell in a flow of reaction gases, then, it was connected to a thermal desorption system with mass spectrometric analysis. After that, the cell was evacuated and heated at a rate of $14\text{ }^\circ\text{C}$ per min. The temperature range of the TPD MS study was $30\text{--}800\text{ }^\circ\text{C}$. Thermal desorption of particles from the surface occurs with different activation energy, the value of which allows to estimate the state of the catalyst surface.

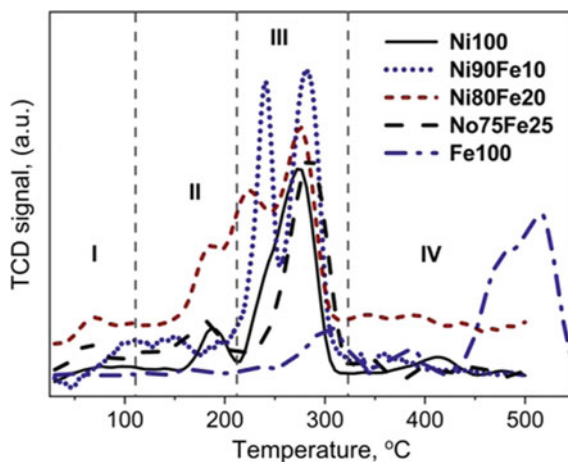
3 Result and Discussion

3.1 Characterization of Bulk NiFe Catalysts

The reducibility of the synthesized monometallic and bimetallic bulk catalysts was investigated by H_2 -TPR. Figure 1 shows the weight-normalized reduction profiles in the temperature range of $50\text{--}550\text{ }^\circ\text{C}$.

The TPR profiles can be divided into four temperature regions that correspond to different thermal transformations of the tested samples (Fig. 1). The first region (Part 1 in Fig. 1, $30\text{--}120\text{ }^\circ\text{C}$) corresponds to weight loss due to water desorption; the second region (Part 2 in Fig. 1, $120\text{--}220\text{ }^\circ\text{C}$) is because of thermal decomposition of Ni and Fe hydroxides with the formation of the corresponding oxides or spinels; the third and fourth regions (Parts 3 and 4 in Fig. 1, above $330\text{ }^\circ\text{C}$) are assigned to the reduction of oxide precursors to the metallic state. The peak positions and intensity of H_2 -TPR profiles (in Parts 1 and 2 in Fig. 1) are similar for monometallic Ni100 and bimetallic NiFe powders. The TPR profiles in Part 3 reflect the weight loss due to the reduction of the metal oxides to respective metals. One peak is characteristic for the Ni100 and Ni75Fe25 powders, while for the Ni90Fe10 and Ni80Fe20 powders, the TPR profile is more complex, which is a sign of a more complex structure of these samples. The TPR profile of the Fe100 powder is different from other ones registered

Fig. 1 H₂-TPR profiles of the monometallic Ni and Fe catalysts, and the bimetallic NiFe bulk catalysts of different compositions



for mono- and bimetallic powders. It is due to the high-temperature resistance of Fe-containing compounds. In the case of the Fe100 powder, on the temperature scale, the weight loss is shifted to a higher temperature (> 500 °C). On the basis of the H₂-TPR results, it can be summarized that 320 °C is the appropriate temperature for reducing prepared oxide precursors up to their metallic state in the process of the bulk NiFe catalyst formation.

The catalytic behavior of the NiFe bimetallic powders with various ratios of metals was evaluated in the temperature range of 150–450 °C. The phase diagram presented in Fig. 2 demonstrates the data of CO₂ conversion and CH₄/CO yield at 350 °C for a number of catalysts. The reasons for good catalytic performance can be analyzed based on the experimental results obtained during the CO₂ methanation over the NiFe bulk catalysts with the different Ni/Fe ratios and the binary phase diagram of Ni–Fe system [35]. We assume that the composition of the most effective catalysts is in the heterogeneous region of the coexistence of γ -Ni(Fe) solid solutions (with 60–70 and 80–100 wt% Ni) and an individual compound FeNi₃. The powder with 75 wt% of Ni and 25 wt% of Fe demonstrates a low methane yield. According to the Ni–Fe phase diagram, the individual compound FeNi₃ exists in the Ni region of 72–77 wt% [36].

The structure and morphology of the surface of Ni80Fe20 and Ni75Fe25 catalysts with high and low catalytic activities, respectively, were investigated by XRD and SEM. After the first stage of synthesis, the examination of the structure of Ni–Fe-containing samples by XRD demonstrates the formation of oxide phases of Ni and Fe (Fig. 3). After successive stages of the reduction of oxide phases by hydrogen and the prepared catalysts used in the CO₂ methanation reaction, the XRD patterns show a subset of reflections corresponding to the cubic face-centered crystalline phase with lattice parameters of 3.54–3.56 Å (Table 1). These values are averaged between those for the monometallic cubic phases of Ni (3.520 Å) and Fe (3.568 Å). This observation may indicate the existence of various cubic face-centered phases, including the FeNi₃ intermetallic compound and the binary Ni–Fe solid solutions [36]. The presence of a

Fig. 2 CH_4/CO production and CO_2 conversion as a function of the Ni content in the composition of the NiFe bulk catalysts and the corresponding phases of the Ni–Fe phase diagram

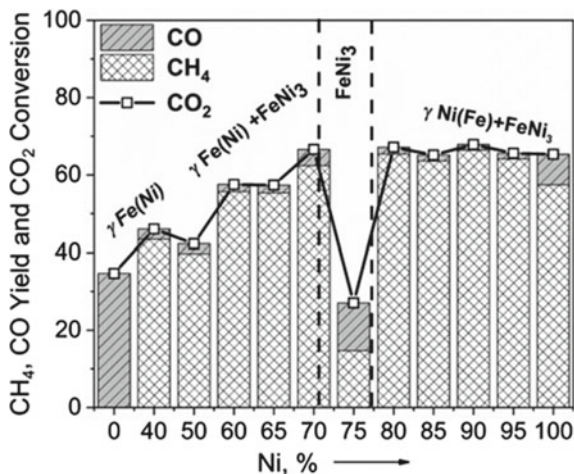
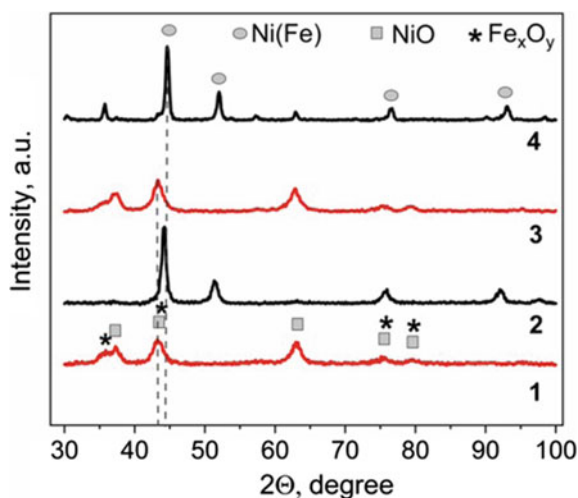


Fig. 3 XRD patterns of Ni₇₅Fe₂₅ (1) and Ni₈₀Fe₂₀ (3) powders in the form of co-precipitated Ni and Fe oxides and after reduction with hydrogen and exposure in the catalytic CO_2 methanation process (2) and (4), respectively



small amount of NiO in the XRD patterns can be explained by passivation. Typically, after the completion of the catalytic reaction, the catalyst samples were subjected to the process of passivation in air, as a result of this procedure metallic catalyst surface was covered with a thin oxide film.

Bulk NiFe catalysts of different compositions have different surface morphology, as demonstrated by the SEM method. Figure 4 proves the significant difference in the microphotographs of individual nickel and iron metals. The nickel surface consists of round-shaped grains with a size of 100–200 nm, which agglomerate into particles of 0.1–0.5 μm , forming a macroporous surface (Fig. 4a, b).

Table 1 XRD data for the NiFe samples in the oxide and metallic forms taken before and after reduction with hydrogen and subsequent exposure in the catalytic CO₂ methanation process, respectively

Sample	Phase	Lattice parameter, Å	Crystallite size, nm
Ni80Fe20 (oxide form)	NiO	4.182	5–7
	Fe ₃ O ₄	8.367	12–19
Ni80Fe20 (metal form)	Ni/Fe	3.537	9–13
Ni75Fe25 (oxide form)	NiO	4.186	5–8
	Fe ₂ O ₃	8.338	5–8
Ni75Fe25 (metal form)	Ni/Fe	3.561	18–23

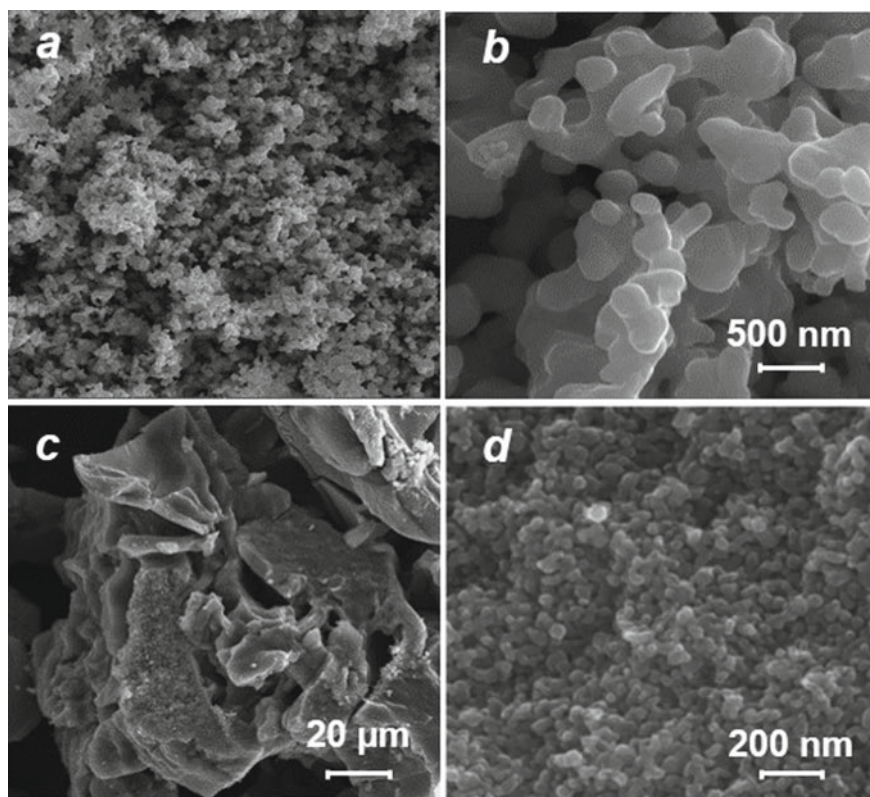
**Fig. 4** SEM images of bulk monometallic **a, b** Ni100 and **c, d** Fe100 catalysts

Figure 4c, d demonstrate that the surface of the monometallic Fe100 catalyst is completely different from that of the monometallic Ni100 one. This catalyst has a smooth flat surface composed of “scales” layered on top of each other. The particles have an irregular shape, with an average size of about 100 μm . During the formation of bimetallic structures, the morphological features of the surface of both nickel and iron are compiled. Figure 5 presents microphotographs of the most effective catalyst (Ni80Fe20) and the sample with the lowest catalytic activity (Ni75Fe25). In fact, that the active Ni80Fe20 catalyst has a highly defective surface compared to inactive one (cf. Fig. 5a, b and 5c, d in pairs).

The Ni80Fe20 catalyst exists as large agglomerates, several tens of microns in size, formed due to the sintering of small spherical particles with a diameter of 80–100 nm. Also, macropores (diameter 100–200 nm) and mesopores (diameter 50 nm) are observed on the microphotograph of the Ni80Fe20 catalyst (Fig. 5b). Contrasting to the Ni80Fe20 catalyst, the SEM images of the Ni75Fe25 catalyst also show large agglomerates with a smooth, non-porous surface (Fig. 5c, d). Agglomerates with such a surface are formed as a result of the sintering of smaller (20–40 nm) metal

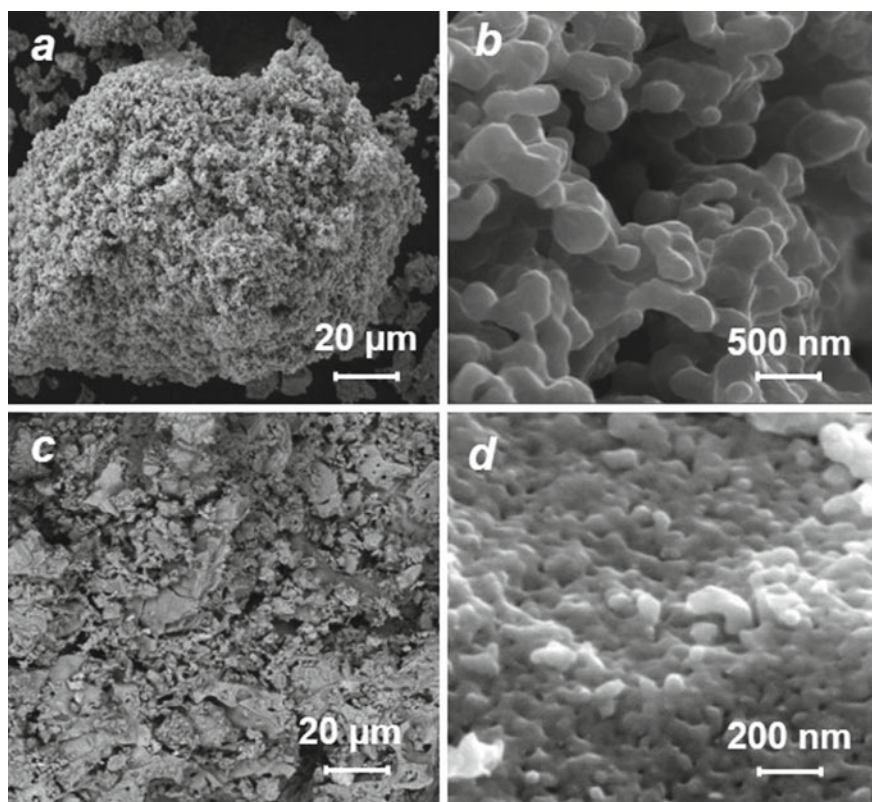


Fig. 5 SEM images of bulk bimetallic **a, b** Ni80Fe20 and **c, d** Ni75Fe25 catalysts

nanoparticles, compared to the active Ni₈₀Fe₂₀ catalyst, with the formation of a denser structure, which negatively affects the catalytic activity of the Ni₇₅Fe₂₅ catalyst.

Figure 6 shows the changes in the relative concentrations of the gas mixture components (CH₄, CO, and CO₂) at the reactor outlet chromatographically recorded during the second temperature rise. For the individual nickel sample, the CO₂ conversion starts at above 200 °C increasing intensively, reaching a maximum of 60% at 400 °C (Fig. 6a). In this case, the main reaction product is methane with a small amount (8%) of CO, the reaction by-products. Adding a small amount of iron (10 wt%) to the Ni-monometallic catalyst significantly affects the CO₂ methanation process, and the conversion of carbon dioxide becomes more rapid. The yield of synthesized methane increases to 63–66%, while the CO yield decreases to 3% (Fig. 6b). A further increase in the concentration of iron content in the catalyst composition to 20 wt% promotes the process of CO₂ hydrogenation to CH₄ (Fig. 6c). However, the formation of CO cannot be excluded completely. The amount of CO (2 vol%) in the gas mixture remains approximately the same in the entire temperature range of the study.

Further studies have shown that the catalytic performance of the Ni₇₅Fe₂₅ catalyst differs considerably from the previously reported catalysts. Figure 6d shows that the CO₂ conversion over the Ni₇₅Fe₂₅ catalyst is significantly lower than found for other NiFe catalysts. As one can see, it reaches a maximum of 25% at 370 °C. At the same time, CH₄ and CO are equally formed in amounts of 12–15 vol%. The reason for this behavior of the NiFe catalyst, consisting of 75 wt% Ni and 25 wt% Fe, should be sought in its structural features. Possibly, the main reason is the formation of the FeNi₃ intermetallic compound that occurs at this ratio of Ni to Fe. In many bimetallic systems, heterogeneous contacts at the interface have an increased catalytic activity compared to homogeneous compositions close to them in chemical composition [37]. Therefore, forming an individual compound with a stoichiometric composition reduces the catalytic activity by default. When the NiFe catalyst contains 50 wt% of iron and above, the CO₂ conversion drops to 40% (Fig. 6e). The CH₄ yield is also significantly reduced. So, the studies of the NiFe catalysts with higher Fe contents in the CO₂ methanation reaction are beyond interest. The Fe₁₀₀ catalyst shows low catalytic performance in this reaction [5, 36]. In its presence, the process selectivity shifts toward the formation of CO, see Fig. 6f.

TPD MS is used to study catalytic processes occurring at the solid–gas interface [38]. This method allows recording the particles desorbed from the solid surface at different temperatures. The resulting TD profiles allow us to assess the state of the catalyst surface during the catalytic reaction, determine the type and state of adsorbed particles on its surface, and propose a model of the reaction mechanism.

The study of the methanation process on bulk NiFe catalysts by TPD MS was carried out on samples with high (Ni₈₀Fe₂₀) and low (Ni₇₅Fe₂₅ and Ni₅₀Fe₅₀) catalytic activities. The thermodesorption temperature maxima (T_m) for all studied samples can be divided into three temperature ranges. The first range is from 50 to 180 °C for species that weakly bound to the catalyst surface; the second is from 200 to 350 °C for species whose desorption occurs at a temperature close to the

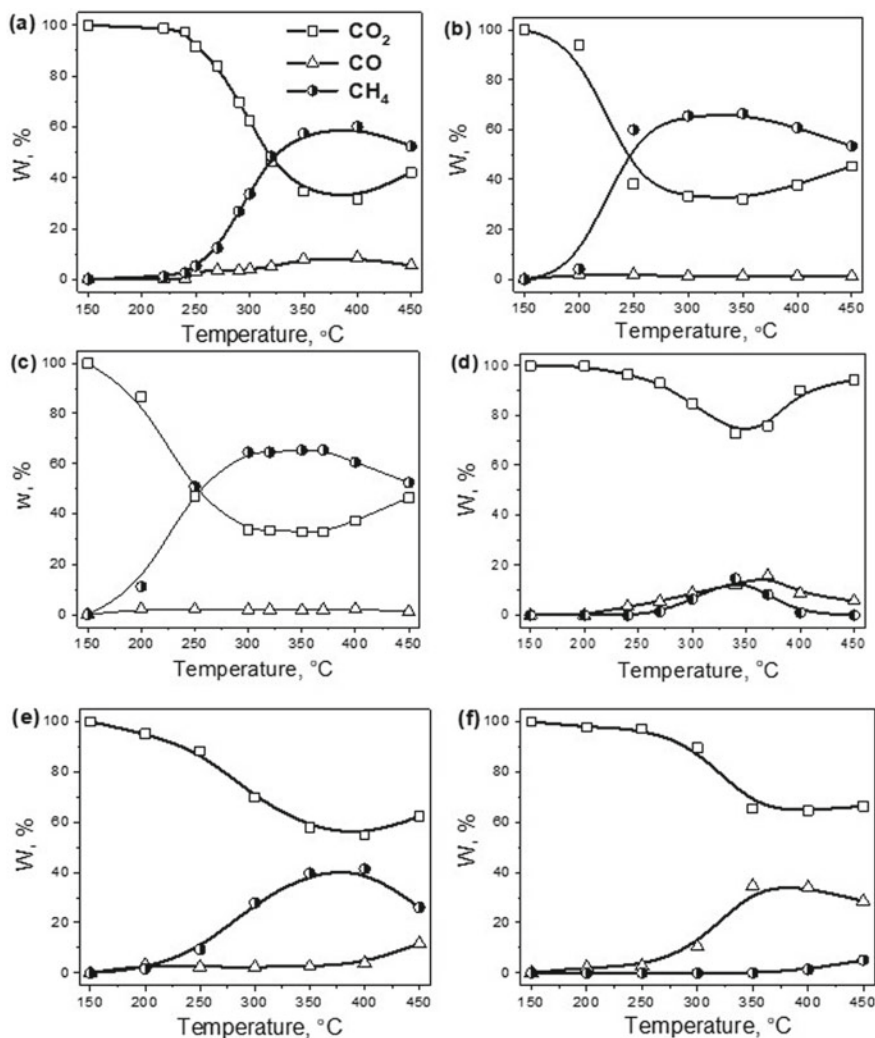


Fig. 6 Volume percentage ($W, \%$) of CH_4 , CO , and CO_2 gases at different temperatures in the outlet gas mixture after catalytic CO_2 methanation using **a** Ni100, **b** Ni90Fe10, **c** Ni80Fe20, **d** Ni75Fe25, **e** Ni50Fe50, and **f** Fe100 catalysts

temperature window of the CO_2 methanation reaction; the third is from 400 to 500 °C for species strongly bound to the catalyst surface.

Figure 7 shows the profiles of CO^* (m/z 28), CO_2^* (m/z 44), and H_2O^* (m/z 18) species desorbed from the Ni80Fe20, Ni75Fe25, and Ni50Fe50 catalysts. It can be seen that for the active Ni80Fe20 catalyst, the TD maxima of CO and CO_2 are registered at $T_m = 100, 150, 300$ °C (Fig. 7a), while the TD spectra of CO^* and CO_2^* from the surface of the Ni75Fe25 and Ni50Fe50 catalysts (Fig. 7b, c) show

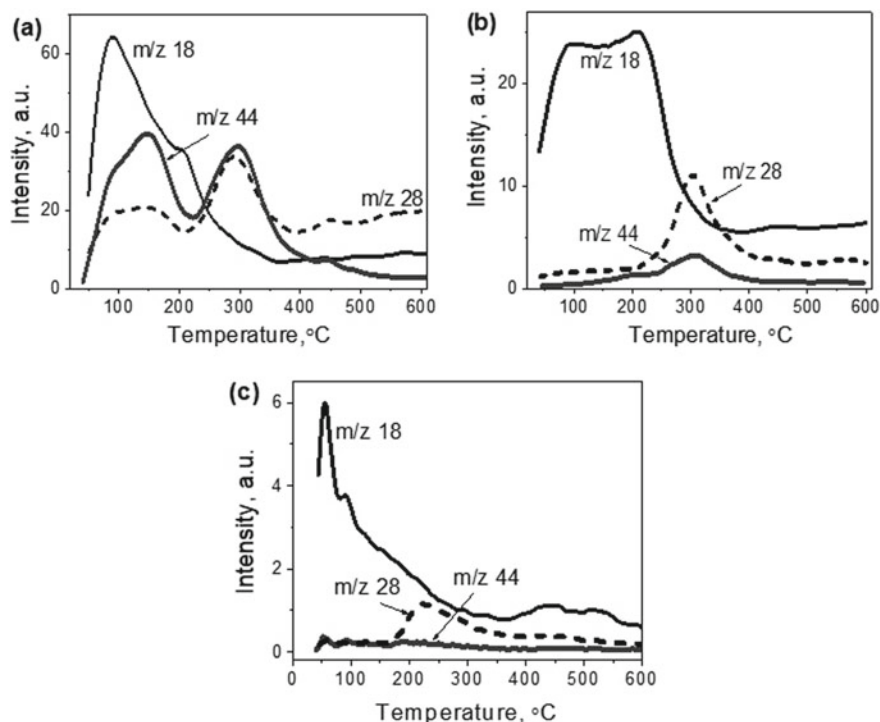


Fig. 7 TD profiles of desorbed species CO₂* (m/z 44), CO* (m/z 28), and H₂O* (m/z 18) from the surface of catalysts **a** Ni₈₀Fe₂₀, **b** Ni₇₅Fe₂₅, and **c** Ni₅₀Fe₅₀ catalysts

only one maximum at 300 °C, and the intensity of the CO peak is much higher than that of CO₂.

According to the data obtained, we assumed that the CO₂ molecule adsorbed on the surface of the Ni₇₅Fe₂₅ sample could decompose into CO* and O*, while CO molecules are strongly chemisorbed on the catalyst surface, preventing future passage of hydrogenation. These results are consistent with the literature data [39, 40], indicating that the process of CO₂ methanation on the surface of catalysts should adsorb CO₂ molecules. Since this process can occur on different active sites of the catalyst with different activation energies, it further affects the reaction mechanism and the composition of the resulting gas mixture.

In Ref. [41], the authors demonstrate that the inactive catalysts are characterized by a single TD peak with T_m in the middle-temperature range, while the CO₂ TD profiles recorded for the active catalysts have several temperature maxima over the entire temperature range. Consequently, different sites for the adsorption of CO₂ are present on the surface of the active catalyst. They are further participating in the pathways of CH₄ formation. Accordingly, the CO₂ conversion and CH₄ yield are high in the presence of such catalysts. This observation is consistent with the results of the study of catalytic activity (Fig. 2). They showed that in the series of the studied

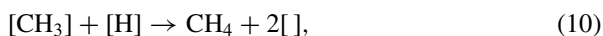
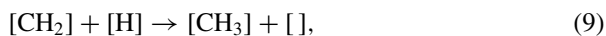
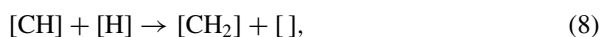
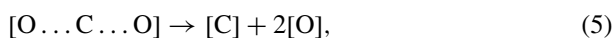
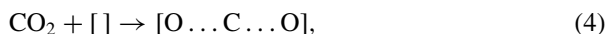
NiFe catalysts, the lowest values of CO₂ conversion and CH₄ yield at a temperature of 300 °C (Fig. 6d) were observed for the Ni75Fe25 catalyst.

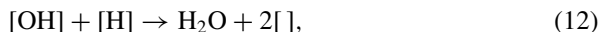
For the active Ni80Fe20 catalyst, the intensity of TD CO₂ and CO profiles is almost the same at 300 °C. The TD profiles of H₂O (m/z 18), which are depicted in Fig. 7, confirm actually that oxygen in the catalytic reaction is produced by dissociated CO₂, not water, over the NiFe catalysts.

These profiles have not peaked in the temperature range of the passage of the catalytic CO₂ methanation reaction. An important observation is the absence of profiles of intermediate oxygen-containing compounds like HCO*, H₂CO*, and others in the TD spectra of the studied samples [36].

Notably, the TD profiles of all desorbed particles from the surface of Ni80Fe20 and Ni75Fe25 have a symmetrical shape. Their desorption from the surface of the catalysts occurs by the dissociative mechanism, when CO, CO₂, and H₂O particles are formed on the catalyst surface layer by recombination from the corresponding atoms [6, 36, 38]. The methanation process on catalysts of this type should include the complete dissociation of the carbon dioxide molecule into separate carbon and oxygen atoms, followed by their interaction with hydrogen and the formation of methane and water, respectively.

Based on the data obtained, one can conclude that the process of CO₂ methanation on the bulk Ni–Fe catalysts can occur by the direct hydrogenation of CO₂ to CH₄. The following scheme depicts the pathways:





where $[\]$ is the free site on the catalyst surface.

In accordance with the above pathways, CO₂ chemisorbed on the active site of the catalyst, which is located at the interface, undergoes complete dissociation to C_{ads}^{*} and O_{ads}^{*} due to the formation of an active complex (Eqs. 4, 5). The adsorbed carbon then reacts rapidly with available hydrogen (from the gas phase or adsorbed on the catalyst surface), resulting in the formation of methane (Eqs. 7–10). Taking into account the fact that nickel is able to adsorb a significant amount of hydrogen with a low activation energy of adsorption [38, 42], the interaction of adsorbed carbon and hydrogen atoms should occur very quickly, which does not allow for registering intermediate CH^{*}, CH₂^{*}, and CH₃^{*} particles in the TD spectra. Water formation occurs by a similar mechanism from adsorbed oxygen and available hydrogen atoms (Eqs. 11, 12). The rate-determining step in this process is most likely the formation of water.

3.2 NiFe Catalysts Loaded on the Carbon Carriers

The most effective method of increasing the activity of the catalyst is its loading on an inert carrier [43, 44]. In this way, it is possible to improve the selectivity of the process for a target product and achieve a higher yield of products or to lower the temperature at their maximum yields. The choice of catalyst carrier to achieve the desired result is an important point in synthesis and further research. Below, the results of the study of the catalytic properties of NiFe catalysts loaded on different carriers are presented. The used carriers can be divided into two groups, namely, carbon and oxide carriers. The carbon carriers include synthetic nanodiamonds (SND), graphite nanoplatelets (GNP), thermally expanded graphite (TEG), and carbon nanotubes (CNTs). All these carriers are characterized by high specific surface area and significant thermal stability.

Loading of the active component on the surface of carbon carriers was carried out by impregnation from nitrate solutions. Studies of catalyst activity in a flow reactor showed a tendency to increase the CH₄ yield with increasing temperature. For catalysts loaded on SND or CNTs, nearly complete conversion of CO₂ occurs at 300 °C, and the catalyst work remains stable up to 400–450 °C. The catalysts based on the GNP and TEG carriers are less active, and in their presence, the minimum temperature of the total CO₂ conversion is registered at 350–375 °C. The behavior of these catalysts is different in the temperature range of 350–450 °C while CO₂ conversion is a maxima. A slight increase of the methane amount over 60%NiFe/GNP catalyst is observed, and methane yield is decreased over 60%NiFe/TEG (Table 2).

This behavior of catalysts is obviously due to the impact of the carbon carrier (GNP or TEG) on the distribution of the active mass on its surface and on the availability of catalytically active sites for the reacting molecules. The GNP has a more ordered

Table 2 Catalytic properties of the NiFe catalysts loaded on carbon carriers

Sample	* $T_1 \rightarrow T_2$, °C	CH ₄ Yield, %	S_{BET} , m ² /g
20% NiFe/SND	300 → 400	78.7 → 90.4	190
20%NiFe/MWCNTs	300 → 400	83.7 → 85.8	140
60%NiFe/MWCNTs	300 → 450	70.2 → 85.4	120
60%NiFe/GNP	375 → 450	70.9 → 71.4	23
60%NiFe/TEG	350 → 450	71.8 → 67.2	50

*The temperature at 100% conversion of CO₂, where T_1 is the temperature at the first analysis point probed at 100% conversion of CO₂, T_2 is the highest temperature over the catalyst exposed in the reaction mixture used for the CO₂ methanation

structure than the TEG, which positively affects the magnetic and conductive properties [45–47]. The SEM photos prove a significant structural difference between TEG and GNP. The TEG has a sponge-like structure [22], while the GNP looks chaotically layered on other plates. These structure features prevent the reactants' access to the active sites on the catalyst. It is because the loaded bimetallic phase is tightly confined inside the TEG honeycombs or between the plates of the GNP. The lack of promising results in the catalytic efficiency of the NiFe/TEG catalyst demonstrates the ineffectiveness of further studies.

More promising are the results of the CO₂ methanation studies over the catalysts loaded on SND and CNTs. The research results presented in [48, 49] show that the NiFe/CNTs and NiFe/SND catalysts provoke of high level of CO₂ conversion and CH₄ yield. For comparison, the activity of the CoFe [5] and the bulk CoNi catalysts [27] is significantly reduced when loaded on the surface of the carbon carrier.

The phase composition of the NiFe/CNTs and the pristine CNTs was studied by the XRD method (Fig. 8). The XRD pattern shows graphite reflections positioned at $2\theta = 30.2^\circ$ (002), 50.5° (100), 52.03° (101), and 63.17° (004) and relative to the pristine CNTs. Also, the XRD pattern shows a weak reflection at $2\theta = 60.9^\circ$ (200) from crystalline Ni contained in the pristine CNTs.

Figure 8b shows a micrograph of the NiFe/CNT samples after their exposure in the CO₂ methanation. The particles of the supported catalytically active phase are located along the entire length of CNTs and in their tangles (see insert in Fig. 8b). Both separate small metal particles and their aggregates can be distinguished. The EDX analysis data of the Ni₈₀Fe₂₀/CNTs catalyst and the calculated ratios show that the amount of the loaded phase at most points of the EDX analysis exceeds the value which is specified at the preparation. Besides, the ratio between the components in the loaded phase becomes variable [49].

The study of the mechanism of the catalytic process on the surface of a nanocomposite catalyst is a difficult task. This statement is especially true when the active mass is localized on the surface of the carrier. The surface of pristine carrier is inert and has no active sites for the activation and interaction of reacted molecules but we can not completely exclude the involvement of the carrier in the catalytic process [13, 23]. Catalyst carriers do not only allow the dispersion of active sites, increasing

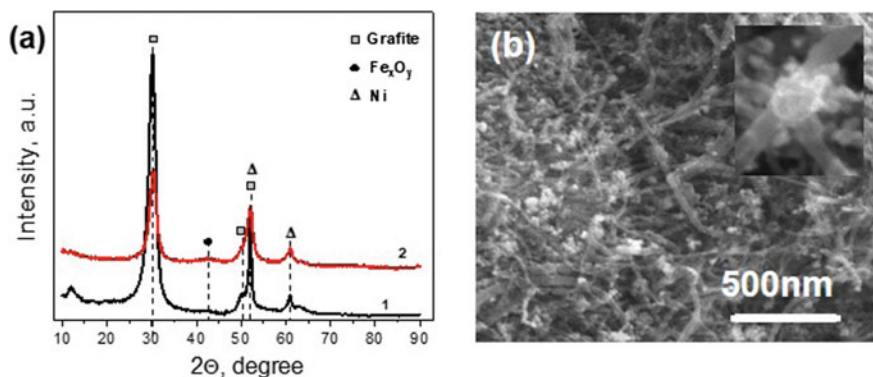


Fig. 8 **a** XRD patterns: (1)—pristine CNTs and (2)—NiFe/CNTs catalyst, **b** SEM micrograph of NiFe/CNTs

the contact area with reagent molecules, but also create an additional opportunity for their adsorption. Of great importance are those areas of the catalyst where the active sites is near the adsorption sites of the carrier surface. In such areas of the catalyst surface, the mechanism of formation of reaction products may differ from the processes occurring on a separate active sites. These conclusions are provided with results of SEM observation of loaded catalysts. Usually, TD profiles of desorbed particles from the surface of such catalysts are multi-peaked, and the separation of individual peaks as the determination of their T_m becomes problematic. We used a specific technique for the TPD MS studies that allows “freezing” the reaction, namely to fix the time when the catalyst surface contains a variety of active sites and adsorbed species with different desorption energies. These sites reflect a certain stage of the catalytic process, i.e., each active site has a specific intermediate “species” adsorbed on it, which is detected by the mass spectrometer during desorption at a certain T_m temperature. Therefore, different intermediate particles corresponding to each stage of the catalytic reaction of the CO₂ methanation are detected in the MS spectra. For the catalysts of 60 wt% NiFe/CNTs and 20 wt% NiFe/CNTs, the desorption of particles with m/z : 44, 30, 29, 28, 16, and 15, corresponding to the (CO₂), (H₂CO*), (HCO*), (CO*), (O*), and (CH₃*) species, takes place in the temperature range of the maximum conversion of CO₂ to CH₄, see Fig. 9a, b. Similar profiles were obtained for the NiFe/SND nanocomposite catalysts [48]. It can explain similar catalytic behavior of CNTs- and SND-based nanomaterials in the CO₂ methanation process.

A nanocomposite catalyst (NC) has a much larger surface for the adsorption of reactant molecules. The elementary acts of the catalytic reaction occur on the surface of the active NiFe bimetallic site. However, the carrier sites with physisorbed CO₂ or H₂ molecules bordering the active catalyst center provide additional adsorption sites that have significantly impacted the formation of intermediate compounds. Under the conditions of the catalytic experiment with excess hydrogen on the catalyst surface, the formation of skeletal hydrocarbons C₂⁺ is unlikely. We can propose the

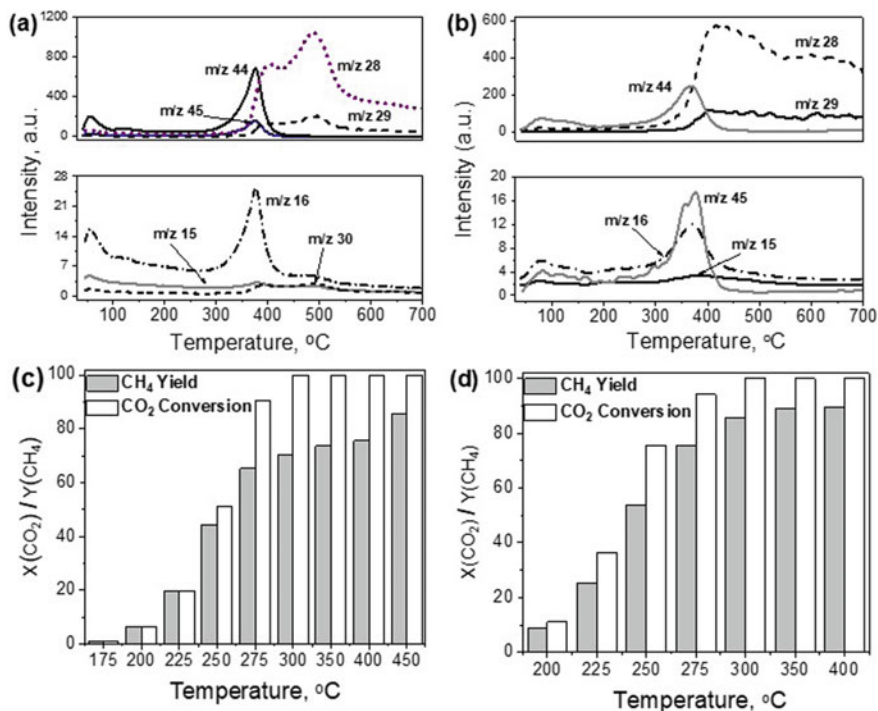


Fig. 9 a, b TPD profiles of desorbed particles from the catalysts and c, d $X(\text{CO}_2)/Y(\text{CH}_4)$ versus temperature

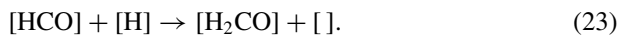
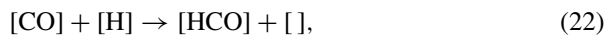
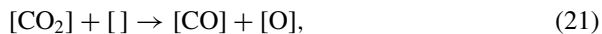
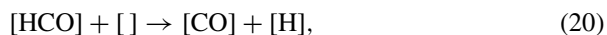
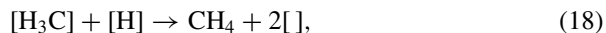
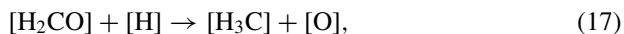
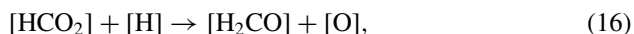
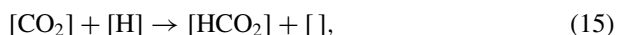
mechanism of CO_2 conversion to CH_4 via intermediate compounds, see Eqs. (13–20). According to the mechanism, CO_2 (m/z 44) and H_2 molecules can be adsorbed on the catalyst active sites (Eqs. 13 and 14). According to Eq. (15), the intermediate compound HCO_2^* (m/z 45) can be formed by adding a hydrogen atom to the adsorbed CO_2 . Further hydrogen adding and oxygen removing lead to the formation of CH_4 (m/z 16), as can be seen from Eqs. (17 and 18).

According to Eqs. (19 and 20), the intermediate compounds: HCO^* (m/z 29) and CO^* (m/z 28) can be formed simultaneously with the main process. The resulting CO^* is not an independent reaction product because we did not register CO molecules by GC. Therefore, the CO^* is desorbed from the surface by a recombination mechanism. These CO^* species can participate in the further process of the CH_4 formation by the reverse reaction, see Eq. (20), or can be strongly adsorbed on the catalyst surface, blocking the active surface sites.

Considering the highly intensive TD profile of m/z 28, the CO^* species can be formed by Eq. (20) and by the decomposition of CO_2 molecules adsorbed on the surface Eq. (21). Further, the reaction proceeds with the addition of a hydrogen atom, see Eqs. (23), (17), and (18). For the sample of 60 wt% NiFe/CNTs, intense CO^* peaks (m/z 28) were recorded at 400 and 500 °C. The intensity of the peak at

500 °C is 30% higher than the peak at 400 °C. For the sample of 20 wt% NiFe/CNTs, the intensity of the CO* peak (m/z 28) becomes maximum in the range of 400–500 °C and then remains at a high level. Thus, CO* desorption occurs from different active sites on the surface. It can be assumed that the presence of a large amount of adsorbed CO* inhibits the catalytic conversion of CO₂ to CH₄.

The GC results show that for the 20 wt% NiFe/CNTs catalyst, the CH₄ yield increases with temperature and reaches the maximum value (89%) at 350 °C. Increasing the amount of Ni₈₀Fe₂₀ active mass on the surface of the carrier to 60 wt% does not lead to an increase in the CH₄ yield in the same temperature range, but on the contrary, decreases it to 76% (Fig. 9c, d). Thus, we have a case when a larger number of active sites can increase the number of intermediate compounds that are strongly chemisorbed on the surface and do not participate in the formation of the targeted product.



3.3 NiFe Catalysts Loaded on Aluminum Oxide Carriers

Bulk Ni₈₀Fe₂₀ catalyst with high conversion rates of CO₂ to CH₄ was loaded on the surface of Al₂O₃ by impregnation. Several types of aluminum oxide with different crystal structures and textural characteristics were used in order to prepare the NiFe nanocomposite (NC) catalysts (Table 3). Before the loading, the carrier was calcined at a temperature of 300–400 °C to remove impurities from the alumina surface. The reduction temperature was estimated by H₂-TPR measurements (Fig. 10). TPR curves have different temperature intervals of weight loss. The reduction of the oxide phase to the metallic state for the NiFe/A3 NC takes place passed at 330 °C. This temperature is similar to that for the bulk catalyst of the same composition. For the NiFe/A2 NC, the reduction process occurs at 250 °C. Obviously, the type of carrier affects the formation of the transition metal oxide phases and their further transformations in the reducing atmosphere.

It was shown in [11, 13] that the reduction of nanooxide precursors to metallic catalysts does not significantly affect the size distribution of pores in the resulting product. Therefore, the formation of a porous structure of the NiFe NCs catalyst based on highly dispersed alumina oxides (with loaded bimetallic active mass) occurs at the stage of localization of metal oxide precursors on the surface of the carrier.

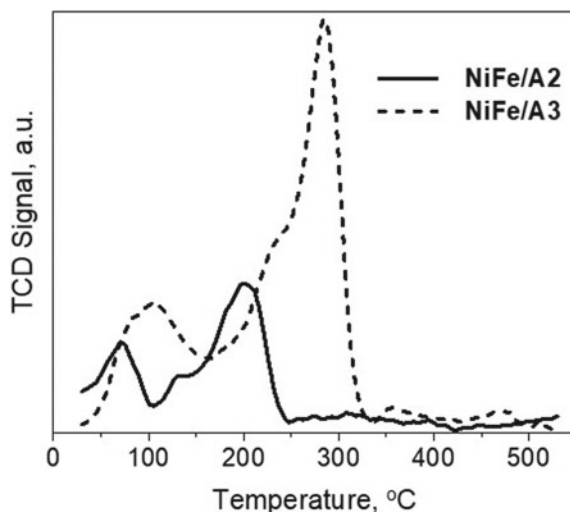
Table 3 Textural characteristics of carriers and catalysts

Sample	^a Specific surface area, m ² g ⁻¹			
	<i>S</i> _{BET}	<i>S</i> _{micro}	<i>S</i> _{meso}	<i>S</i> _{macro}
Al ₂ O ₃ (A1)	106.4	6.7	99.3	0.4
NiFe/A1	83.4	4.0	78.9	0.5
Al ₂ O ₃ (A2)	46.8	2.5	43.1	1.2
NiFe/A2	37.9	1.2	35.7	1.1
Al ₂ O ₃ (A3)	210.5	32.8	176.7	1.0
NiFe/A3	145.4	33.4	111.7	0.2

Sample	<i>R</i> _{p,v}	Specific volume, cm ³ g ⁻¹			
		<i>V</i> _p	<i>V</i> _{micro}	<i>V</i> _{meso}	<i>V</i> _{macro}
Al ₂ O ₃ (A1)	6.5	0.219	0.004	0.206	0.009
NiFe/A1	8.1	0.166	0.002	0.153	0.011
Al ₂ O ₃ (A2)	14.6	0.203	0.002	0.170	0.031
NiFe/A2	14.5	0.159	0.001	0.132	0.026
Al ₂ O ₃ (A3)	11.3	0.579	0.014	0.542	0.023
NiFe/A3	4.8	0.203	0.013	0.186	0.004

^aSpecific surface area in total (*S*_{BET}), of nanopores (*S*_{nano}), mesopores (*S*_{meso}), macropores (*S*_{macro}), and pore volumes (*V*_p, *V*_{nano}, *V*_{meso}, *V*_{macro}) at pore radius *R* < 1nm, 1nm < *R* < 25nm, and *R* > 25 nm, respectively. *R*_{p,v} represents the average pore radius [50]

Fig. 10 H₂-TPR profiles for Ni₈₀Fe₂₀/A2 and Ni₈₀Fe₂₀/A3 NCs



Clearly, the structural characteristics of the alumina carrier play a crucial role in the formation of the active centers of the NiFe catalyst and their surface distribution. Three types of aluminum oxide were used to load the active NiFe composition. All of them are characterized by different specific surface areas and by different porosities. The porous structures of types A1 and A2 carriers have preferable mesoporosity with a minor contribution of macropores. The alumina carrier of type A3 is a mesoporous–microporous sorbent. The prepared NCs catalysts, where NiFe bimetallic active mass is loaded on the alumina surface, have the different resulting textures.

The nitrogen adsorption-desorption isotherms for the NiFe/A1 and NiFe/A2 NCs and the corresponding pore size distribution data are similar to the initial alumina (A1 and A2) carriers (Fig. 11a, c). According to the IUPAC classification, they belong to the L2 type, and the corresponding hysteresis loops belong to the H3 type. The NCs based on the A1 and A2 carriers show a decrease in adsorption capacity. This decrease is due to a shortage in the total volume of pores. At the same time, the ratio of micropores, mesopores, and macropores does not change significantly. The nitrogen adsorption isotherm measured for the NiFe/A3 NC differs significantly from that of the respective A3 carrier (Fig. 11e). The hysteresis loops observed for the A3 carrier and for the NiFe/A3 NC can be classified as type H3 and H4 hysteresis loops, respectively [51].

Figure 11b, d, f show the incremental distribution of pores by size calculated from the nitrogen adsorption isotherm. All carriers and related NCs have a predominantly mesoporous structure. For the NCs based on A1 and A2 carriers, micro- and macropores do not contribute much to the total porosity; factually, their contribution is either insignificant or absent. In contrast, a contribution of micropores in the total porosity of the NCs based on the A3 carrier is recognizable. Notably, the A3 carrier has a more developed specific surface area of 210 m² g⁻¹ in contrast to the A2 and A1 carriers.

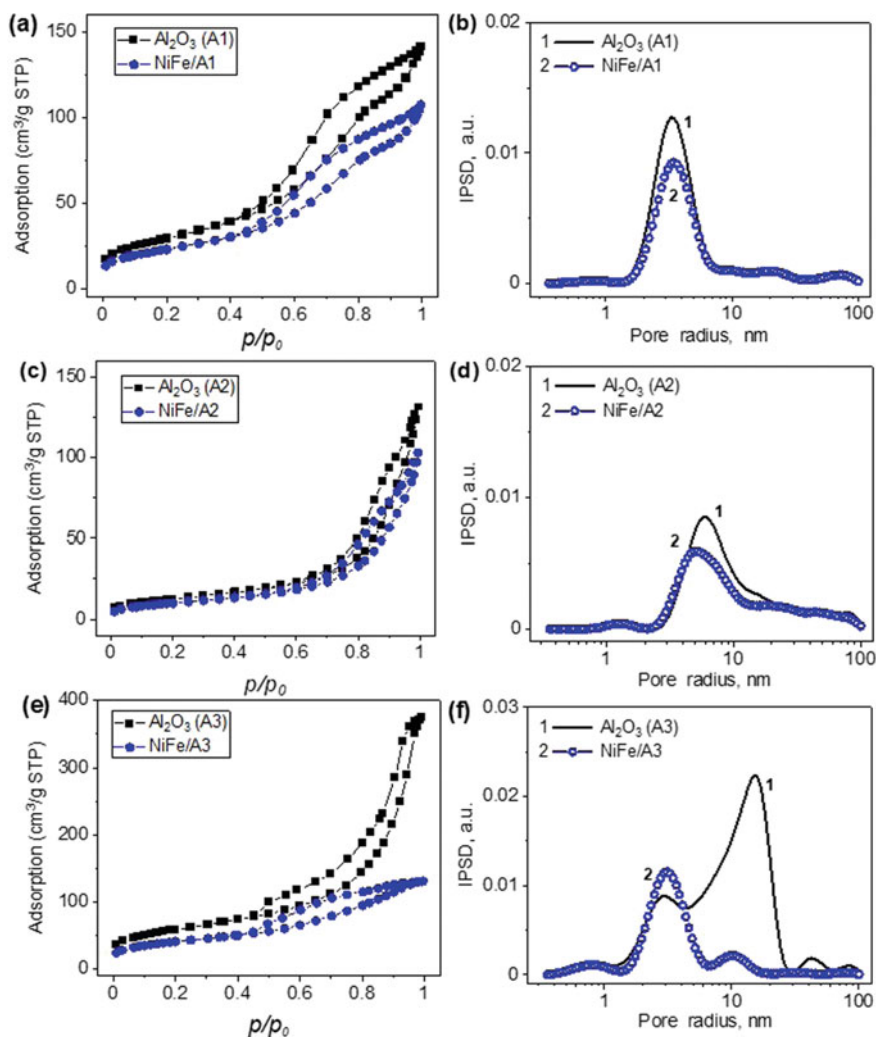


Fig. 11 a–f Textural parameters of alumina (A1–A3) carriers (1) and NiFe/(A1–A3) NCs (2): a, c, e nitrogen adsorption/desorption isotherms and b, d, f incremental pore size distributions

However, after a load of bimetallic NiFe particles, the specific surface area of the resulting NC based on the A3 carrier decreases more than that of the NCs based on the A1 or A2 carriers after the same operation. The specific surface area of the NiFe/A3 NC is lesser by 30% than that of the A3 carrier (cf. 145 and 211 $\text{m}^2 \text{g}^{-1}$ in Table 3). Moreover, the distribution of pores by size also changes after loading the NiFe particles. The specific porosity decreases entirely and precisely at the expense of mesopores available in the A3 carrier. If one compares the contribution of mesopores to the total porosity of the A3 carrier and the NiFe/A3 NC based on it, it will be clear

that it is less by 38% for the latter. From another hand, in comparison with the A3 carrier, the fraction of micropores for the NiFe/A3 NC is slightly higher.

As one can see from Table 3, after loading of nanoscale bimetallic NiFe particles on the A2 or A1 carrier, the specific surface area of the resulting NCs is 22% lesser than that of the respective carrier (cf. 106 to 83 m² g⁻¹ and 47 to 38 m² g⁻¹ in Table 3). In contrast, the specific surface area of NiFe/A3 NC is 30% lesser than that of the A3 carrier.

Furthermore, the respective NiFe/A3 and NiFe/A2 NCs maintain a preferable mesoporosity. In fact, the contribution of micropores and macropores to the total porosity is equally insignificant for both A1 and A2 carriers and composites based on them.

The calculated incremental pore size distributions for the A3 and NiFe/A3 NC demonstrate a part of microporosity in the structure of the A3 carrier. A ratio for this type of pore increases for the NiFe/A3 nanocomposite if referenced with that for the A3 carrier.

Obviously, the related pore size distribution changed significantly. The ratio of mesopores with sizes of 2–8 nm increased. However, the contribution of mesopores with a radius up to 40 nm, as in the A3 carrier, is practically absent (Fig. 11f).

The crystal structure of the initial carriers, as well as their textural characteristics, has differences and affects the formation of the loaded catalyst active mass. XRD patterns of the studied carriers and the related NCs (Fig. 12) demonstrate the differences between the crystalline structure of the A2 and A3 carriers and the registered reflections of loaded metals. The XRD patterns of the alumina carriers were recorded using the CuK α radiation, and the CoK α radiation was used to record the XRD patterns for the nanocomposite catalysts with the loaded NiFe active phase.

The crystal lattice of the A2 carrier contains the reflections of α - and γ -modifications of alumina (Fig. 12 a). One can see the broadening of the reflexes peaked at $2\theta = 52.85^\circ$ and 59.9° and assigned to α -Al₂O₃ and γ -Al₂O₃ phases. This situation is possible due to the superposition of the reflection of the metallic nickel.

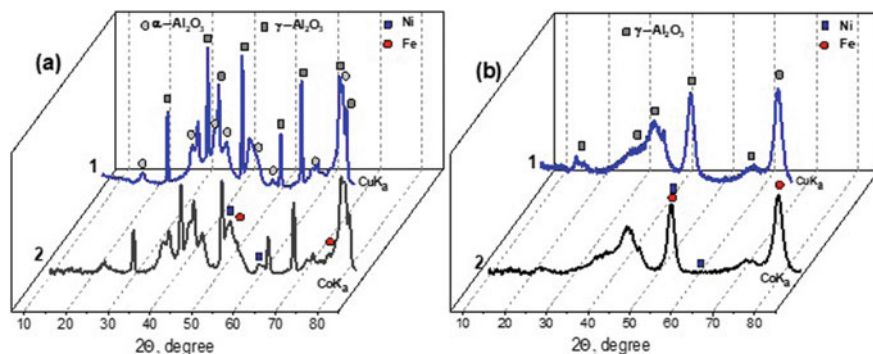


Fig. 12 XRD patterns of **a** Ni80Fe20/A2 and **b** Ni80Fe20/A3 NCs (curve 1) and the respective carriers (curve 2)

The presence of metallic iron is proved by the appearance of shoulders for two reflections centered at $2\theta = 54.75^\circ$ and 79.5° (Fig. 12a). The structure of the carrier A3 has features typical for the $\gamma\text{-Al}_2\text{O}_3$ crystal lattice exclusively. The reflection assigned to the metallic nickel phase is registered only at $2\theta = 52.85^\circ$. The reflections of the metallic iron phase are identified at $2\theta = 54.75^\circ$ and 79.5° .

The surface morphology of the used carriers is different. The A2 carrier is composed of large agglomerates of particles 10–50 μm in size. Additionally, on the SEM micrographs (Fig. 13a), small non-aggregated particles of 3–7 μm in size are visible. They have the shape of irregular tetragonal or pentagonal prisms, the surface of which has defects in the form of cracks located on the side faces. Inclusions of small particles, the size of which does not exceed 3 μm , are also visible in the cracks. This structure is typical for the surface of high-temperature $\alpha\text{-Al}_2\text{O}_3$ [44]. The A3 carrier ($\gamma\text{-Al}_2\text{O}_3$) has no distinct individual particles. Its surface has a loose structure due to an aggregation of nanoscale particles (Fig. 13b). Such surface morphology explains the significant difference in the values of the specific surface area of the studied carriers, namely, 46 and 210 m^2/g for $\alpha\text{-}$ and $\gamma\text{-Al}_2\text{O}_3$, respectively.

The surface morphology of $\alpha\text{-Al}_2\text{O}_3$ (A2) does not change significantly because of the active phase loading. The SEM micrograph shows that the active phase in the

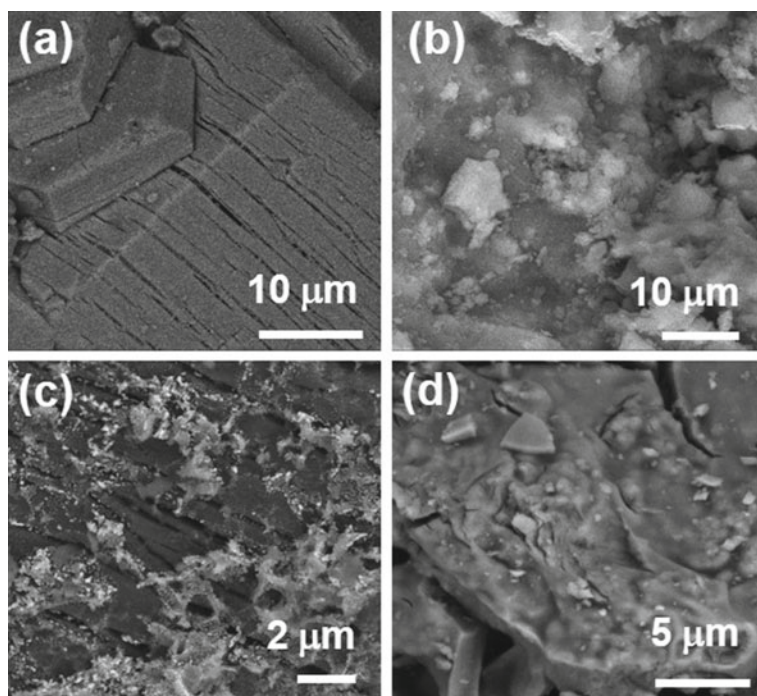


Fig. 13 SEM micrographs of **a** A2 and **b** A3 carriers and NCs based on them **c** NiFe/A2 and **d** NiFe/A3

Ni80Fe20/A2 NC catalyst is like a “net”. This net covers some agglomerates of the carrier (Fig. 13c).

Typically, the loaded Ni80Fe20 particles do not penetrate the surface cracks characteristic of α -Al₂O₃. But, they are localized on the geometric surface of the carrier and are available for further catalytic CO₂ methanation. Comparing the SEM micrographs of the surface of γ -Al₂O₃ before and after the loading of the active phase, we consider that in the preparation of the Ni80Fe20/ γ -Al₂O₃ NC catalyst, the structure of the carrier surface undergoes significant changes. Thus, in (Fig. 13d), we observed the absence of graininess and, consequently, high dispersion, which is observed for the initial γ -Al₂O₃. The NC catalyst surface is smooth and comprises with small fragments ranging in size from 200 nm to several microns. They are chaotically placed on the carrier surface and maybe the fragments of the loaded active phase. The EDX analysis (Table 4) shows that the ratio between the components in the bimetallic active phase for the Ni80Fe20/A2 NC catalyst remains within limits specified at the preparation: Ni (80 wt%)-Fe (20 wt%). For the Ni80Fe20/ γ -Al₂O₃ NC catalyst, the related metal content in the Ni80Fe20 active mass is 26–42 at.% of Fe to 74–58 at.% of Ni. So, the iron-enriched areas can be recorded with the EDX analysis. In our opinion, increasing the amount of Fe on the surface decreases catalytic activity and promotes the formation of CO molecules.

An important question is how the difference in the textural characteristics of the carrier and its crystal structure affects the catalytic properties of the studied NC catalysts. The catalytic activity of alumina-based NCs catalysts was evaluated with the same procedure as for the bulk catalysts. GC results of the evaluation of CO₂ conversion over NiFe/Al₂O₃ nanocomposites (including A1, A2, and A3 carriers) are presented in Fig. 14.

The GC analysis results indicate the intensive CO₂ conversion into CH₄ at 200 °C in the presence of the Ni80Fe20/A1 and Ni80Fe20/A2 NC catalysts. The total CO₂ conversion occurs at 275 and 250 °C in the presence of Ni80Fe20/A1 and Ni80Fe20/A2 catalysts respectively. But, the Ni80Fe20/A3 catalyst does not show similar catalytic activity. The presented dependences demonstrate an obvious difference in the impact of the type of carrier on the catalytic activity of the loaded active NiFe mass. When the active phase is loaded on α -Al₂O₃, this has a significant positive effect. And the total conversion of CO₂ and 100% selectivity toward CH₄ are

Table 4 EDX analysis results

Ni80Fe20/A2				Ni80Fe20/A3			
EDX, at. %				EDX, at. %			
O	Al	Fe	Ni	O	Al	Fe	Ni
47.3	31.6	3.9	17.2	66.2	28.7	1.4	3.8
42.9	29.9	9.1	18.0	66.2	27.8	2.5	3.5
61.8	34.4	0.9	2.9	66.2	31.0	1.1	1.7
61.4	35.9	0.6	2.1	66.7	29.2	1.3	2.9

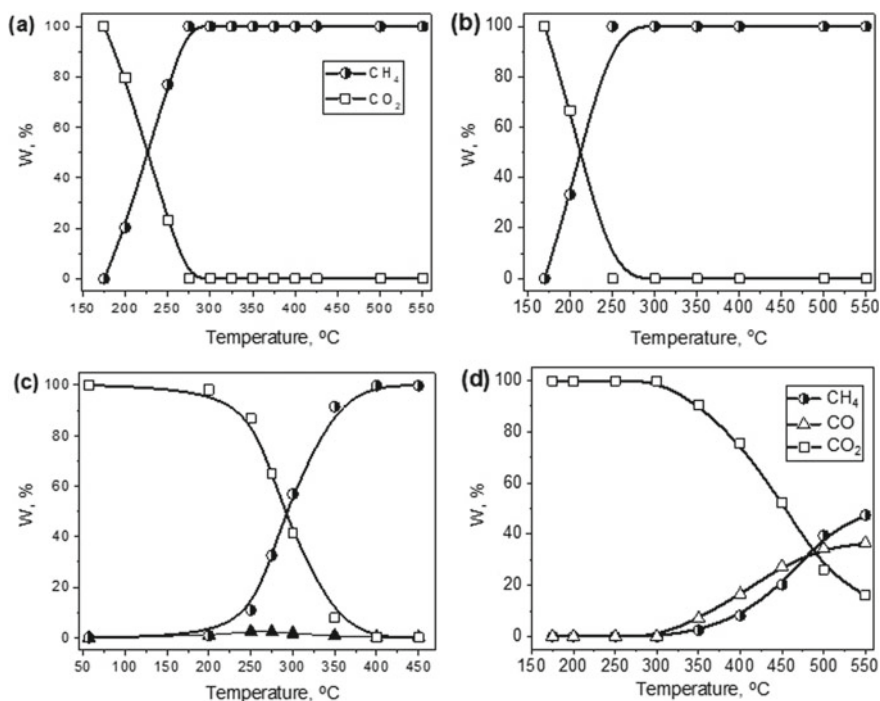


Fig. 14 Temperature dependence of the volume percentage of CH₄, CO, and CO₂ (W, %) for the CO₂ methanation over **a** Ni80Fe20/A1, **b** Ni80Fe20/A2, **c** Ni50Fe50/A2, and **d** Ni80Fe20/A3 NC catalysts

observed at 250 °C (Fig. 14a–c). For the γ -Al₂O₃ carrier, the CO₂ conversion is 80–90%, while CO is GC detected as the reaction co-product (Fig. 14d).

For the Ni80Fe20/A3 NC catalyst, the CO₂ methanation reaction begins at above 300 °C. That is why the maximum conversion (88%) of the initial CO₂ is observed at 550 °C (Fig. 14c). The amount of CO obtained between 350 and 450 °C exceeds the amount of CH₄, the maximum yield of which reaches 50 vol % at high temperature.

As can be seen from the above data, the highest activity is shown by the catalysts loaded on α -Al₂O₃ (A1 and A2 carriers). Fig. 14 demonstrates the course of the temperature profiles where the catalytic activity depends not only on the type of carrier but also on the ratio of components in the active NiFe phase. As seen from Fig. 14c and b, for the Ni50Fe50/A2 NC catalysts, the total conversion of CO₂ to CH₄ is observed at 400 °C. But, for the Ni80Fe20/A2 NC catalyst, this temperature is much lower at about 250 °C.

It is clear that the structural, textural, and morphological features of the studied carriers determine the properties of the resulting alumina-based bimetallic nanocomposites. The porosity of the carrier determines the localization of the loaded active mass. The use of aluminum oxide (A3) as a catalyst carrier causes the adsorption of catalytic active metal phases in micropores, as a result the active phase becomes

partially inaccessible to reactant molecules from the gas phase. The TPR profiles and catalytic performance approved this observation.

The porous structure of NCs based on the A1 and A2 carriers is characterized by preferable mesoporosity. These carriers have a small number of macropores. Both types of pores contribute to the efficient course of the CO₂ methanation reaction. The mesopores are the principal working pores of the prepared catalysts for the molecules interaction. Macropores are the way to deliver reactant molecules that can fill the inner volume of the NCs catalyst. As a result, the catalytic processes can occur not only on the outer surface of the catalyst grains but also inside the inner porous volume. In the NiFe/A3 NC catalyst, the micropores prevent the catalytic processes since the metal particles trapped in the micropores become inaccessible to the reactant molecules and cannot be involved in catalysis.

4 Conclusion

The bulk NiFe catalysts with a nickel content in the range of 60–70 wt% and 80–95 wt% showed the high catalytic activity in the reaction of CO₂ methanation. The addition of iron (5–20 wt%) to the catalyst composition significantly increases its catalytic efficiency compared to the monometallic nickel catalyst. The highest CO₂ conversion and CH₄ yields were registered for the catalyst with the composition of Ni (80 wt%)–Fe (20 wt%). The formation of intermetallic FeNi₃ compound in the Ni75Fe25 catalyst, which surface is enriched with iron, leads to a rapid decrease of catalytic activity. The analysis of TD profiles of desorbed species from the surface of bulk NiFe catalysts indicates the CO₂ methanation reaction occurs due to the complete breakdown of CO₂ molecules (splitting into carbon and oxygen atoms) and the formation of CH₄ by the recombination mechanism with the gradual addition of hydrogen atoms to the carbon atoms.

Loading the active mass of NiFe catalyst with the ratio of Ni (80 wt%)–Fe (20 wt%) on the surface of carbon and alumina carriers causes 100% CO₂ conversion.

The selectivity of CH₄ formation and the temperature of complete CO₂ conversion on loaded catalysts depend on the nature of the carrier on which loaded the active NiFe mass. Among carbon carriers, nanocomposite NiFe/CNTs catalysts showed high activity of CO₂ conversion into CH₄. The distribution of the active mass of NiFe catalyst along the carbon nanotube bundles and their localization in the nodes contributes to the efficient formation of CH₄ at atmospheric pressure and 350 °C on the catalyst containing 20 wt% of Ni80Fe20. Increasing the amount of active mass to 60 wt% does not increase the CH₄ yield. The formation of CH₄ occurs by a mechanism via formation of oxygen-containing HCO₂*[•], H₂CO*[•], and HCO*[•] species.

The study of the activity of alumina-based NiFe NCs catalysts demonstrated that the catalytic efficiency of the CO₂ methanation depends on the textural characteristics of the carrier.

The microporosity of the Al_2O_3 carrier (A3) has a negative impact on the conversion of CO_2 to CH_4 due to the loss of a part of active catalyst sites unavailable for the CO_2 methanation reaction passage due to their possible localization in the micropores. The ordered crystal structure of $\alpha\text{-Al}_2\text{O}_3$ promotes the formation of the NiFe catalytically active sites.

References

1. M. Götz, J. Lefebvre, F. Mörs, A. McDaniel Koch, F. Graf et al., Renewable power-to-gas: a technological and economic review. *Renew. Energy* **85**, 1371–1390 (2016). <https://doi.org/10.1016/j.renene.2015.07.066>
2. K. Hashimoto, M. Yamasaki, K. Fujimura, T. Matsui et al., Global CO_2 recycling—novel materials and prospect for prevention of global warming and abundant energy supply. *Mater. Sci. Eng. A* **267**, 200–206 (1999). [https://doi.org/10.1016/S0921-5093\(99\)00092-1](https://doi.org/10.1016/S0921-5093(99)00092-1)
3. J. Lefebvre, M. Götz, S. Bajohr, R. Reimert, T. Kolb, Power-to-Gas through thermal integration of high-temperature steam electrolysis and carbon dioxide methanation—experimental results. *Fuel Process. Technol.* **132**, 83–90 (2015). <https://doi.org/10.1016/j.fuproc.2014.10.040>
4. P. Strucks, L. Failing, S. Kaluza, A short review on Ni-catalyzed methanation of CO_2 : reaction mechanism, catalyst deactivation, dynamic operation. *Chem. Ing. Tech.* **93**, 1526–1536 (2021). <https://doi.org/10.1002/cite.202100049>
5. O.V. Ischenko, A.G. Dyachenko, I. Saldan, V.V. Lisnyak, V.E. Diyuk, A.V. Vakaliuk, A.V. Yatsymyrskiy, S.V. Gaidai, T.M. Zakharova, O. Makota, T. Ericsson, L. Häggström, Methanation of CO_2 on bulk Co-Fe catalysts. *Int. J. Hydrog. Energy* **46**, 37860–37871 (2021). <https://doi.org/10.1016/j.ijhydene.2021.09.034>
6. R. Meshkini Far, O.V. Ischenko, A.G. Dyachenko, O. Bieda, S. Gaidai, V. Lisnyak, CO_2 hydrogenation into CH_4 over Ni-Fe catalysts. *Funct. Mater. Lett.* **11**, 1850057 (2018). <https://doi.org/10.1142/S1793604718500571>
7. Y.R. Dias, O.W. Perez-Lopez, CO_2 conversion to methane using Ni/ SiO_2 catalysts promoted by Fe, Co and Zn. *J. Environ. Chem. Eng.* **9**(1), 104629 (2021). <https://doi.org/10.1016/j.jece.2020.104629>
8. A.V. Yatsymyrskiy, A.G. Dyachenko, E.V. Ischenko, T.M. Zakharova, S.V. Gaidai, V.E. Diyuk, V.V. Lisnyak, Carbon dioxide molecular interactions with hydrogenated Ni(111) surface: a DFT study. *Molec. Cryst. Liq. Cryst.*, in press (2022). <https://doi.org/10.1080/15421406.2022.2073032>
9. M. Zhlyudenko, A. Dyachenko, O. Bieda, S. Gaidai, M. Filonenko, O. Ischenko, Structure and catalytic properties of Co-Fe systems in the reaction of CO_2 methanation. *Acta Physica Polonica A* **133**, 1084 (2017). <https://doi.org/10.12693/APhysPolA.133.1084>
10. G. De Piano, J.J.A. Gambo, A.M. Condó, S. Bengió, F.C. Gennari, Bimetallic Ni-Fe catalysts for methanation of CO_2 : effect of the support nature and reducibility. *Appl. Catal. A: Gen.* **634**, 118540 (2022). <https://doi.org/10.1016/j.apcata.2022.118540>
11. A. Dyachenko, O. Ischenko, V. Diyuk, O. Goncharuk, M. Borysenko, O. Mischanchuk, T. Zakharova, O. Pryhunova, D. Sternik, V. Lisnyak, The catalytic efficiency of Fe-containing nanocomposites based on highly dispersed silica in the reaction of CO_2 hydrogenation. *Res. Chem. Intermediat.* **48**, 2607–2625 (2022). <https://doi.org/10.1007/s11164-022-04720-x>
12. S.V. Gaidai, V.S. Gryn'ko, M.G. Zhlyudenko, A.G. Dyachenko, V.M. Tkach, O.V. Ischenko, Activity of carbon-fiber-supported Fe-Co catalysts in the CO_2 methanation reaction. *J. Superhard. Mater.* **39**, 122–128 (2017). <https://doi.org/10.3103/S1063457617020071>
13. A. Dyachenko, O. Ischenko, O. Goncharuk, M. Borysenko, O. Mischanchuk, V. Gun'ko, D. Sternik, V. Lisnyak, Preparation and characterization of Ni-Co/ SiO_2 nanocomposite catalysts for CO_2 methanation. *Appl. Nanosci.* **12**, 349–358 (2022). <https://doi.org/10.1007/s13204-020-01650-1>

14. O. Goncharuk, O. Shipul, A. Dyachenko, O. Ischenko, L. Andriyko, A. Marynin, E. Pakhlov, O. Oranska, M. Borysenko, Silica-supported Ni and Co nanooxides: Colloidal properties and interactions with polar and nonpolar liquids. *J. Molec. Liq.* **285**, 397–402 (2019). <https://doi.org/10.1016/j.molliq.2019.04.127>
15. O. Linnik, E. Manuilov, S. Snegir, N. Smirnova, A. Eremenko, Photocatalytic degradation of tetracycline hydrochloride in aqueous solution at ambient conditions stimulated by gold containing zinc-titanium oxide films. *J. Adv. Oxid. Technol.* **12**, 265–270 (2009). <https://doi.org/10.1515/jaots-2009-0218>
16. O. Linnik, I. Petrik, N. Smirnova, V. Kandyba, O. Korduban, A. Eremenko, G. Socol, N. Stefan, C. Ristoscu, I.N. Mihailescu, C. Sutan, V. Malinovsky, TiO₂/ZrO₂ thin films synthesized by PLD in low pressure N-, C- and/or O-containing gases: structural, optical and photocatalytic properties. *Digest J. Nanomater. Biostruct.* **7**, 1343–1352 (2012)
17. P.R. Yaashikaa, P.S. Kumar, S.J. Varjani, A. Saravanan, A review on photochemical, biochemical and electrochemical transformation of CO₂ into value-added products. *J. CO₂ Util.* **33**, 131–147 (2019). <https://doi.org/10.1016/j.jcou.2019.05.017>
18. V.Y. Zabuga, O.O. Bochechka, G.G. Tsapyuk, V.E. Diyuk, A.M. Panova, V.V. Lisnyak, On multiwalled carbon nanotubes oxidation: Thermogravimetric, spectral and macrokinetic studies. *Molec. Cryst. Liq. Cryst.* **661**(1), 81–90 (2018). <https://doi.org/10.1080/15421406.2018.1460257>
19. I. Sulym, O. Goncharuk, D. Sternik, K. Terpilowski, A. Derylo-Marczewska, M.V. Borysenko, V.M. Gun'ko, Nanooxide/polymer composites with Silica@PDMS and Ceria–Zirconia–Silica@PDMS: textural, morphological, and hydrophilic/hydrophobic features. *Nanoscale Res. Lett.* **12**, 152 (2017). <https://doi.org/10.1186/s11671-017-1935-x>
20. D. Sternik, M.V. Galaburda, V.M. Bogatyrov, O. Oranska, B. Charnas, V.M. Gun'ko, Novel porous carbon/clay nanocomposites derived from kaolinite/resorcinol-formaldehyde polymer blends: synthesis, structure and sorption properties. *Appl. Surf. Sci.* **52530**, 146361 (2020). <https://doi.org/10.1016/j.apsusc.2020.146361>
21. E.V. Ischenko, V.K. Yatsimirsky, A.G. Dyachenko, M.V. Borysenko, E.V. Prilutskiy, I.V. Kongurova, Cu-Co-Fe oxide catalysts supported on carbon nanotubes in the reaction of CO oxidation. *Polish J. Chem.* **82**, 291–297 (2008)
22. E.V. Ischenko, L.Y. Matzui, S.V. Gayday, L.L. Vovchenko, T.V. Kartashova, V.V. Lisnyak, Thermo-exfoliated graphite containing CuO/Cu₂(OH)₃NO₃:(Co²⁺/Fe³⁺) composites: preparation, characterization and catalytic performance in CO conversion. *Materials* **3**, 572 (2010). <https://doi.org/10.3390/ma3010572>
23. G.G. Tsapyuk, V.E. Diyuk, R. Mariychuk et al., Effect of ultrasonic treatment on the thermal oxidation of detonation nanodiamonds. *Appl. Nanosci.* **10**, 4991–5001 (2020). <https://doi.org/10.1007/s13204-020-01277-2>
24. S.M. Hwang, C. Zhang, S.J. Han, H.G. Park, Y.T. Kim, S. Yang et al., Mesoporous carbon as an effective support for Fe catalyst for CO₂ hydrogenation to liquid hydrocarbons. *J. CO₂ Util.* **37**, 65–73 (2020). <https://doi.org/10.1016/j.jcou.2019.11.025>
25. A.G. Dyachenko, O.V. Ischenko, M.V. Borysenko, S.V. Gaidai, A.V. Yatsymyrskiy, G.G. Tsapyuk, O.V. Pryhunova, O.O. Kostyrko, Co-Fe/Al₂O₃ Nanocomposite catalysts of the process of CO₂ hydrogenation. *Theor. Experim. Chem.* **58**, 134–142 (2022). <https://doi.org/10.1007/s11237-022-09731-8>
26. O. Goncharuk, A. Dyachenko, E. Skwarek, O. Ischenko, L. Andriyko, M. Borysenko, I. Sulym, D. Sternik, K. Kowalska, M. Marynin, Structure of aluminosilicate-supported nickel and iron oxides nanocomposites in gaseous and aqueous media. *Physicochem. Probl. Miner Process.* **58**(2), 144375 (2022). <https://doi.org/10.37190/ppmp/144375>
27. O.V. Ishchenko, A.G. Dyachenko, A.V. Yatsymyrskiy, T.M. Zakharova, S.V. Gaidai, V.V. Lisnyak, R. Mariychuk, CO₂ methanation over Co-Ni catalysts. *E₃S Web Conf.* **154**, 02001 (2020). <https://doi.org/10.1051/e3sconf/202015402001>
28. A.G. Dyachenko, O.V. Ischenko, M.G. Zhudenko, S.V. Gaidai, T.M. Zakharova, A.V. Yatsymyrskiy, V.V. Lisnyak, CO₂ methanation over Co–Ni/Al₂O₃ and Co–Ni/SiC catalysts. *Bulg. Chem. Commun.* **52**, 342–347 (2020). <https://doi.org/10.34049/bcc.52.3.5134>

29. T. Xie, J. Wang, F. Ding, A. Zhang, W. Li, X. Guo et al., CO₂ hydrogenation to hydrocarbons over alumina-supported iron catalyst: effect of support pore size. *J. CO₂ Util.* **19**, 202–208 (2017). <https://doi.org/10.1016/j.jcou.2017.03.022>
30. T. Numpilai, N. Chanlek, Y. Poo-Arporn, S. Wannapaiboon, C.K. Cheng, N. Siri-Nguan et al., Pore size effects on physicochemical properties of Fe-Co/K-Al₂O₃ catalysts and their catalytic activity in CO₂ hydrogenation to light olefins. *Appl. Surf. Sci.* **483**, 581–592 (2019). <https://doi.org/10.1016/j.apsusc.2019.03.331>
31. J. Rouquerol, F. Rouquerol, K.S.W. Sing, P. Llewellyn, G. Maurin, *Adsorption by Powders and Porous Solids: Principles, Methodology and Applications*, 2nd edn. (Academic Press, Amsterdam, 2013), p.646
32. S.J. Gregg, K.S.W. Sing, *Adsorption, Surface Area and Porosity* (Academic Press, London, 1982), 303 p
33. A. Monshi, M. Foroughi, R. Monshi, Modified Sherrer equation to estimate more accurately nano-crystallite size using XRD. *World J. Nano Sci. Eng.* **2**, 154–160 (2012). <https://doi.org/10.4236/wjnse.2012.23020>
34. V.L. Veselovskiy, E.V. Ischenko, S.V. Gayday, V.V. Lisnyak, A high efficient two phase CuO/Cu₂(OH)₃NO₃(Co²⁺/Fe³⁺) composite catalyst for CO-PROX reaction. *Catal. Commun.* **18**, 137–141 (2012). <https://doi.org/10.1016/j.catcom.2011.11.024>
35. M.L. Cubeiroa, H. Morales, Hydrogenation of carbon oxides over Fe/Al₂O₃ catalysts. *Appl. Catal. A.: Gen.* **189**, 87–97 (1999). [https://doi.org/10.1016/S0926-860X\(99\)00262-8](https://doi.org/10.1016/S0926-860X(99)00262-8)
36. R. Meshkini Far, A. Dyachenko, S. Gaidai, O. Bieda, M. Filonenko, O. Ishchenko, Catalytic properties of Ni-Fe systems in the reaction of CO₂ methanation at atmospheric pressure. *Acta Physica Polonica A.* **133**, 1088–1090 (2018). <https://doi.org/10.12693/APhysPolA.133.1088>
37. V.L. Budarin, V. Dnyuk, L. Matzui, L. Vovchenko, T. Tsvetkova, M. Zakharenko, New prospective Ni-catalytic materials. *J. Thermal Anal. Calorim.* **62**, 345–348 (2000). <https://doi.org/10.1023/A:1010140803562>
38. R.J. Cvetanović, Y. Amenomiya, Application of a temperature programmed desorption technique to catalyst studies. *Adv. Catal.* **17**, 103–149 (1967). [https://doi.org/10.1016/S0360-0564\(08\)60686-0](https://doi.org/10.1016/S0360-0564(08)60686-0)
39. N. Nishimura, S. Kitaura, A. Mimura, Y. Takahara, Cultivation of thermophilic methanogen KN-15 on H₂–CO₂ under pressurized conditions. *Ferment Bioeng.* **73**, 477–480 (1992). [https://doi.org/10.1016/0922-338X\(92\)90141-G](https://doi.org/10.1016/0922-338X(92)90141-G)
40. S. Fujita, H. Terunuma, M. Nakamura, N. Takezawa, Mechanisms of methanation of carbon monoxide and carbon dioxide over nickel. *Ind. Eng. Chem. Res.* **30**, 1146–1151 (2002). <https://doi.org/10.1021/ie00054a012>
41. X. Guo, D. Gao, H. He, A. Traitangwong, M. Gong, V. Meeyoo, Z. Peng, C. Li, Promotion of CO₂ methanation at low temperature over hydrotalcite-derived catalysts-effect of the unable metal species and basicity. *J. Hydrog. Energy* **46**, 518–530 (2021). <https://doi.org/10.1016/j.ijhydene.2020.09.193>
42. K.S.W. Sing, D.H. Everett, H. Raw, L. Moscou, R.A. Pierotti, J. Rouquerol, T. Siemieniewska, Reporting physisorption data for gas/solid systems with special reference to the determination of surface area and porosity. *Pure Appl. Chem.* **54**(11), 2201–2218 (1982). <https://doi.org/10.1351/pac198254112201>
43. M.A.A. Aziz, A.A. Jalil, S. Triwahyono, S.M. Sidik, Methanation of carbon dioxide on metal-promoted mesostructured silica nanoparticles. *Appl. Catal. A Gen.* **486**, 115–122 (2014). <https://doi.org/10.1016/j.apcata.2014.08.022>
44. M. Trueba, S. Trasatti, γ -alumina as a support for catalysts: a review of fundamental aspects. *Eur. J. Inorg. Chem.* **17**, 3393–3403 (2005). <https://doi.org/10.1002/ejic.200500348>
45. L.Y. Matzui, L.L. Vovchenko, O.A. Syvolozhskiy, O.S. Yakovenko, M.O. Borovoy, O.O. Gomom, A.G. Dyachenko, O.V. Ischenko, A.V. Vakaliuk, A.V. Bodnaruk, V.M. Kalita, Structure and magnetic properties of MWCNTs decorated by NiFe, CoFe, NiCo nanoparticles. *Molec. Cryst. Liq. Cryst.* **752**, 74–94 (2023). <https://doi.org/10.1080/15421406.2022.2091275>
46. O.S. Yakovenko, L.Y. Matzui, O.A. Syvolozhskiy, L.L. Vovchenko, O.A. Lazarenko, O.V. Ischenko, A.G. Dyachenko, A.V. Vakaliuk, V.V. Oliynyk, V.V. Zagorodnii, A.V. Bodnaruk,

- V.M. Kalita, M.O. Borovoy, Epoxy composites filled with graphite nanoplatelets modified by FeNi nanoparticles: structure and microwave properties. *Mater. Sci. Eng. B* **283**, 115776 (2022). <https://doi.org/10.1016/j.mseb.2022.115776>
47. L.Y. Matzui, O.A. Syvolozhskiy, Y.O.S. Vovchenko, O.A. Lazarenko, T.A. Len, O.V. Ischenko, A.G. Dyachenko, A.V. Vakaliuk, V.V. Oliynyk, V.V. Zagorodnii, Electrical and electromagnetic interference shielding properties of GNP-NiFe hybrid composite with segregate structure of conductive networks. *J. Appl. Phys.* **131**, 055110 (2022). <https://doi.org/10.1063/5.0071157>
48. A.G. Dyachenko, O.V. Ischenko, G.G. Tsapyuk, S.V. Gaidai, O.V. Ischenko, T.M. Zakharova, G.D. Il'nitskaya, O.B. Loginova, Synthetic nanodiamonds (SNDs) containing bimetallic Ni(Co)-Fe composites: preparation, characterization and catalytic performance in the reaction of CO₂ methanation. *Molec. Cryst. Liq. Cryst.* **701**, 91–97 (2020). <https://doi.org/10.1080/15421406.2020.1732566>
49. A.G. Dyachenko, O.V. Ischenko, O.V. Prygunova, V.E. Diyuk, G.G. Tsapyuk, S.V. Gaidai, A.V. Yatsymyrskiy, T.M. Zakharova, E.O. Kostyrko, Ni-Fe, Co-Fe, and Co-Ni nanocomposites based on carbon nanotubes in the reaction of CO₂ methanation. *Molec. Cryst. Liq. Cryst.* **702**, 38–46 (2021). <https://doi.org/10.1080/15421406.2021.1905281>
50. V.M. Gun'ko, Composite materials: textural characteristics. *Appl. Surf. Sci.* **307**, 444–454 (2014). <https://doi.org/10.1016/j.apsusc.2014.04.055>
51. M. Thommes, K. Kaneko, A.V. Neimark, J.P. Olivier, F. Rodriguez-Reinoso, J. Rouquerol, K.S.W. Sing, Physisorption of gases, with special reference to the evaluation of surface area and pore size distribution (IUPAC Technical Report). *Pure Appl. Chem.* **87**, 1051–1069 (2015). <https://doi.org/10.1515/pac-2014-1117>